Crystallinity Dynamics of Gold Nanoparticles During Sintering or Coalescence

Eirini Goudeli and Sotiris E. Pratsinis
Dept. of Mechanical and Process Engineering, Particle Technology Laboratory, Institute of Process Engineering, ETH Zürich, Sonneggstrasse 3, CH-8092 Zürich, Switzerland

DOI 10.1002/aic.15125
Published online December 22, 2015 in Wiley Online Library (wileyonlinelibrary.com)

The crystallinity of gold nanoparticles during coalescence or sintering is investigated by molecular dynamics. The method is validated by the attainment of the Au melting temperature that increases with increasing particle size approaching the Au melting point. The morphology and crystal dynamics of nanoparticles of (un)equal size during sintering are elucidated. The characteristic sintering time of particle pairs is determined by tracing their surface area evolution during coalescence. The crystallinity is quantified by the disorder variable indicating the system's degree of disorder. The atoms at the grain boundaries are amorphous, especially during particle adhesion and during sintering when grains of different orientation are formed. Initial grain orientation affects final particle morphology leading to exposure of different crystal surfaces that can affect the performance of Au nanoparticles (e.g., catalytic efficiency). Coalescence between crystalline and amorphous nanoparticles of different size results in polycrystalline particles of increasing crystallinity with time and temperature. Crystallinity affects the sintering rate and mechanism. Such simulations of free-standing Au nanoparticle coalescence are relevant also to Au nanoparticles on supports that do not exhibit strong affinity or strong metal support interactions. © 2015 American Institute of Chemical Engineers *AIChE J*, 62: 589–598, 2016

Keywords: crystallinity, sintering rate, gold, coalescence, molecular dynamics

Introduction

Gold nanoparticles find a score of applications including catalysis,[1] plasmonic biosensing,[2] target-specific drug-delivery,[3] nanolithography,[4] and ion detection.[5] However, their size, shape, composition, and crystal structure strongly affect final product properties and eventually performance, especially below 10 nm where particles' behavior differs both from that of the bulk metal and the Au molecules.[6] For example, small nanoparticles are more attractive as catalysts than larger ones due to their increased defects and edges or steps leading to higher activity and selectivity.[7]

Nanoparticles are produced either by liquid-[8] or gas-phase methods.[9] Even though the most prevalent method for synthesis of gold nanoparticles is in the wet-phase (Turkevich method[10]), gas-phase processes offer distinct advantages over liquid-phase ones in scale-up, product purity (e.g., optical fibers) and particle handling.[11] However, during gas-phase synthesis (e.g., aerosol reactors) high temperatures are encountered, so coagulation and sintering/coalescence are the dominant particle growth mechanisms controlling product particle size and morphology. Recent advances in gas-phase synthesis have allowed close control of collision and sintering rates and, therefore, particle size and shape through selection or tuning of process parameters, though little is known about detailed sintering kinetics and crystallinity dynamics during coalescence.[12] The particles' crystal structure at the nanoscale is important in electronics as it affects ion/electron transport properties, in catalysis where atomic steps and kicks enhance catalytic activity[7] and in molecular sensing devices where monocrystalline nanoparticles can optimize performance.[13] Furthermore, nanograined polycrystalline materials are brittle[14] because motion of dislocations is suppressed by nanocrystallites. Thus, there is a need to engineer nanomaterial morphology and crystallinity for tailoring catalytic, electronic, and mechanical properties to improve product and even device performance.

Molecular dynamics (MD) have unraveled the evolution of morphology or shape of various nanomaterials during coalescence (e.g., Cu[15]; Au[16]; Al[17]; Si[18]; Ag[19]; TiO_2[20]) and even the detailed sintering rate of TiO_2[21] or Ag crystalline structure.[22] Here, the sintering mechanism and nanocrystallinity of coalescing Au nanoparticles is investigated by graphics processing unit (GPU)-accelerated atomistic MD simulations. The method is validated by the attainment of the Au melting temperature as a function of particle size and its bulk melting point. The characteristic sintering time of particle pairs is determined by tracing their surface area evolution during coalescence.[21] The state of crystallinity is quantified by the deviation of each gold atom from its location in a perfect face cubic centered (fcc) crystal describing that way the system's degree of disorder. Sintering results in multiple grains (polycrystalline particles) that are wiped out and transform into a single crystal

Additional Supporting Information may be found in the online version of this article.

Correspondence concerning this article should be addressed to S. E. Pratsinis at sotiris.pratsinis@ptl.mavt.ethz.ch.

© 2015 American Institute of Chemical Engineers

at sufficiently long times. The results are compared with electron beam irradiation experiments of coalescing Au nanoparticles.[23] Besides free-standing Au nanoparticle coalescence, these simulations are quite relevant also to sintering of Au on ceramic oxide supports that do not exhibit strong affinity[24] or metal support interactions, such as Ag on TiO_2.[25]

Theory

Molecular dynamics

Spherical Au nanoparticles were extracted from a large fcc crystal with lattice constant 4.078 and different cutoff (particle) diameters, $d_{p,0} = 1.5$–11 nm (114–41,186 atoms). An fcc crystal that occupies the entire cubic simulation domain (with edge of 10 nm) applying periodic boundary conditions is considered here as bulk. These fcc crystals were equilibrated at 300 K for 1 ns and continuously heated up to 1600 K for 5 ns. The equations of motion are integrated by the velocity-Verlet algorithm[26] with a timestep of 1 fs. Two unsupported (free) nanoparticles of equal size are placed next to each other for sintering in vacuum (after 1 ns of equilibration at the sintering temperature, T) with a separation distance of 0.3 nm between the closest atom centers and sintering simulations are performed in the NVT (constant number, volume and temperature) ensemble with $T = 500$–1000 K. Coalescing nanoparticles of different size (Figure 9) are equilibrated for 1 ns at 800 (crystalline) or 1000 K (amorphous) and sinter at constant $T = 800$ K (equivalent to annealing). Here the many-body embedded-atom method (EAM) potential[27,28] is used with the parameterization of Foiles et al.[29] The total energy, E_{tot}, is

$$E_{\text{tot}} = \sum_i F_i\left(\rho_{h,i}\right) + \frac{1}{2}\sum_{i,j\neq i}\phi(r_{ij}) \tag{1}$$

where F_i is the embedding term accounting for the local electron density, $\rho_{h,i}$, r_{ij} is the distance between atoms i and j, and $\phi(r_{ij})$ is the potential for pairwise interactions between gold atoms. The simulations are performed on GPUs for up to 100 ns using the LAMMPS[30] MD code.

Characteristic sintering time

When particles are placed next to each other, fusion takes place to minimize the system's free energy resulting in particle rounding by reduction of the free surface area. The evolution of the surface area is determined using the MSMS 6.2.1[31] which calculates the solvent-accessible area of overlapping spheres. The probe radius is set equal to 2.25 Å corresponding to that of a N_2 molecule while the van der Waals radius of gold atoms is 1.66 Å.[32] This method of surface area calculation corresponds to the standard technique of specific surface area measurement by N_2 adsorption.[33]

The characteristic sintering time, τ_s, is the time required for the neck radius to reach 83% of the initial particle radius,[34] corresponding to 67% reduction of the excess surface area over that of a fully coalesced sphere with equivalent volume or to 86.7% of the equivalent coalesced sphere area. The rate of change of the surface area by sintering is[35]

$$\frac{da}{dt} = -\frac{1}{\tau_s}(a - a_s) \tag{2}$$

where α_s is the surface area of a fully fused aggregate. Coalescence of gold nanoparticles has been investigated both theoretically[16,36] and experimentally (e.g., by tandem differential mobility analyzer[37]). Liu et al.[38] studied the coalescence of Au nanoclusters by MD and high resolution electron microscope. They reported that at high temperatures the dominant sintering step is the collapse of local surfaces and migration of disordered surface atoms. In contrast, at lower temperatures coalescence occurs by a dislocation mechanism based on high shear stresses that develop between particles. Arcidiacono et al.[36] found that gold nanoparticles larger than 4 nm in diameter coalesce by grain boundary diffusion. Similarly, Buesser et al.[21] observed that surface diffusion is the dominant sintering mechanism up to 5 nm in diameter of TiO_2 with grain boundary diffusion becoming important with increasing particle size. The characteristic sintering time by surface diffusion is[39]

$$\tau_s = \frac{k_B T r_{p,0}^4}{CD\gamma a^4} \tag{3}$$

where k_B is the Boltzmann constant, T (K) is the temperature, $r_{p,0}$ (m) is the particle radius, C is a constant ($C = 25$[40]), D (m^2/s) is the diffusion coefficient, γ (N/m^2) is the surface tension and α (m) is the atomic size. Yuk et al.[23] observed by *in situ* transmission electron microscope (TEM) images of electron beam irradiated Au nanoparticles (3–7 nm) that they sinter by oriented attachment which occurs either by three-dimensional particle orientation or by grain boundary migration, depending on particles' contact orientation.

Crystallinity dynamics

The disorder of a system was first quantified by Steinhardt et al.[41] with the so-called bond order parameters (or Steinhardt parameters), q_{lm}, which are measures of the local and extended orientational symmetries of the particles

$$q_{lm}(i) = \frac{1}{N_b(i)}\sum_{j=1}^{N_b(i)} Y_{lm}(\mathrm{r}_{ij}) \tag{4}$$

where $N_b(i)$ is the number of nearest neighbors around particle i, $Y_{lm}(r_{ij})$ are the spherical harmonic functions of degree l and $-l \le m \le l$. Here, $l = 6$ as Au nanoparticles are arranged in an fcc crystal structure.[42] Equation 4 can be improved so that the local crystal structure is detected and effectively described by the averaged local bond order parameters[43]

$$\bar{q}_{lm}(i) = \frac{1}{N_b(i)}\sum_{j=1}^{N_b(i)} q_{lm}(j) \tag{5}$$

Thus, the extent of disorder of the system is given by the disorder variable[42]

$$D_i(t) = \frac{1}{N_b(i)}\sum_{j=1}^{N_b(i)}\sum_{m=-l}^{l}\left|q_{lm}(i,t) - q_{lm}(j,t)\right|^2 \tag{6}$$

and the overall disorder variable, $\bar{D}$, is the average D_i over all atoms

$$\bar{D}(t) = \sum_{i=1}^{N}\frac{D_i(t)}{N - N_b(i)} \tag{7}$$

where N is the total number of atoms. Small values indicate an fcc-like crystal structure and big ones a more disordered environment. $\bar{D}$ is close to unity for glassy or liquid materials and decreases significantly for crystal structures.[42]

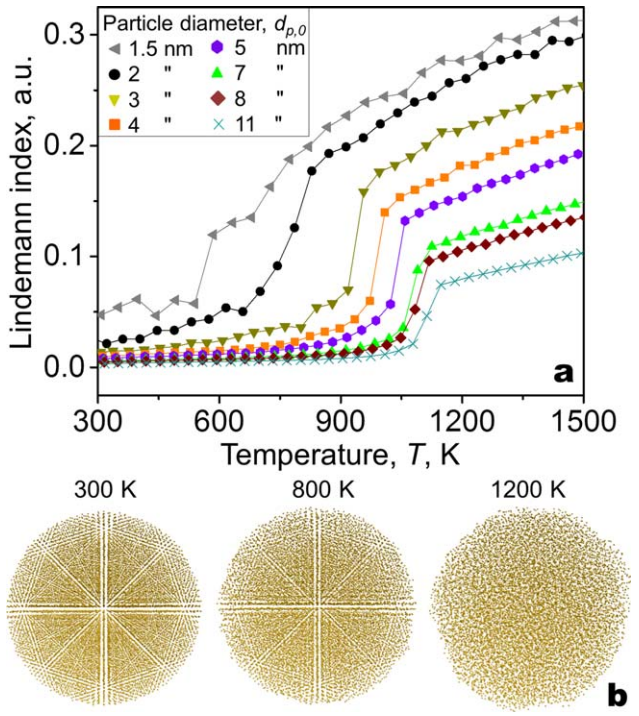

Figure 1. (a) Evolution of the average Lindemann index of Au particles of various diameters as function of temperature during heating from 300 to 1600 K for 5 ns.

The Lindemann index abruptly increases during the transition to highly disordered systems (liquid-like state) indicating melting. The melting temperature, T_m, is defined as the temperature where that abrupt increase of the Lindemann index ends (e.g., at 1000 K for $d_{p,0} = 3$ nm). (b) Snapshots of Au nanoparticles with $d_{p,0} = 8$ nm at $T = 300$, 800, and 1200 K. As temperature increases, the perfect Au fcc structure ($T = 300$ K) fades away inwards from the surface: at $T = 800$ K the surface atoms are in a liquid-like state whereas the core ones maintain their fcc-like structure until the entire particle becomes liquid at $T = 1200$ K. [Color figure can be viewed in the online issue, which is available at wileyonlinelibrary.com.]

Results and Discussion

Validation: Melting temperature

The MD simulations are benchmarked by calculating the melting temperature of nanosized Au nanoparticles (particle diameter, $d_{p,0} = 1.5$–11 nm) by the Lindemann index method which is used to trace the thermally driven disorder of a system. The root-mean-squared bond length fluctuation, δ_i, of atom i is[44]

$$\delta_i = \frac{1}{N-1} \sum_{j \neq i} \frac{\sqrt{\langle r_{ij}^2 \rangle - \langle r_{ij} \rangle^2}}{\langle r_{ij} \rangle} \tag{8}$$

and the system-averaged Lindemann index, δ, is

$$\delta = \frac{1}{N} \sum_i \delta_i \tag{9}$$

The brackets denote the thermal average at temperature T. An abrupt increase of the Lindemann index indicates phase transition from the solid to liquid state and the corresponding temperature is the melting point. Similarly, the melting point is also identified by the jump in the potential energy.

Figure 1a shows the evolution of the system-average Lindemann index (Eq. 9) of Au particles with diameter, $d_{p,0} = 1.5$–11 nm, as function of temperature during heating from 300 to 1600 K for 5 ns. At low temperatures, the Lindemann index is small (less than 0.05) but abruptly increases for highly disordered systems (liquid-like state) indicating melting. During this transition the solid and liquid phases dynamically coexist. The melting temperature, T_m, is defined here as the temperature where that steep increase of the Lindemann index ends (e.g., at about 1150 K for $d_{p,0} = 5$ nm). The Lindemann index for most particles exhibits a sharp increase but for the smallest ones (i.e., the 1.5 and 2 nm in diameter) it increases gradually with temperature. These particles consist of a few hundred atoms (e.g., 114 and 250 for the 1.5 and 2 nm ones, respectively) that contain dominantly (~60–80%) atoms on the particle surface, a low coordination number and rather amorphous state that is akin to fluid-like behavior. This leads to a gradual or gentle increase of the Lindemann index with increasing temperature (Figure 1). In contrast, the behavior of larger particles with increasing temperature is dominated by their bulk atoms. These particles exhibit a narrow bistable region as has been observed also during melting of aluminum nanoparticles (Alavi and Thomson:[45] Figures 3 and 4).

Figure 1b shows snapshots of the Au nanoparticles with $d_{p,0} = 8$ nm at $T = 300$, 800 and 1200 K (corresponding Lindemann index, Figure 1a: diamonds). Initially, at $T = 300$ K the particle retains the almost perfect fcc structure but when temperature increases ($T = 800$ K) the perfect Au fcc structure ($T = 300$ K) fades away inwards from the surface: at $T = 800$ K the surface atoms are in amorphous or liquid state (layer of disordered atoms) whereas the core (bulk) ones maintain their fcc-like structure. At even higher temperatures the layer of highly distorted surface atoms increases in thickness until all atoms completely lose their crystal structure ($T = 1200$ K) when the melting point is exceeded.

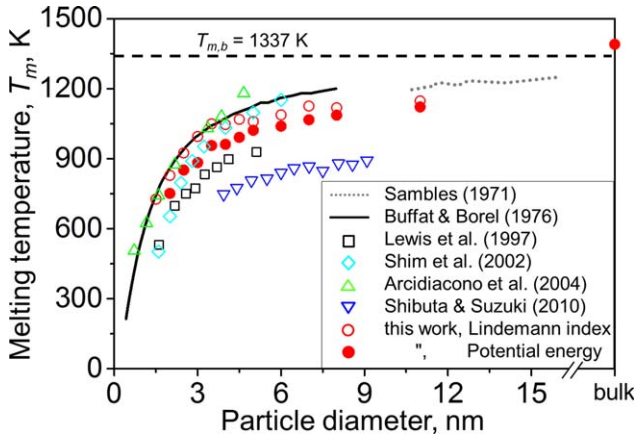

Figure 2. Melting temperature, T_m, of Au nanoparticles obtained by the Lindemann index (open circles) and the change in potential energy (filled circles) as a function of their diameter, $d_{p,0}$, in comparison to experimental data (solid and dotted lines) and simulations (symbols).

For a large Au cube with a 10 nm edge the melting temperature is in good agreement with the bulk melting point of $T_{m,b} = 1337$ K (broken line). [Color figure can be viewed in the online issue, which is available at wileyonlinelibrary.com.]

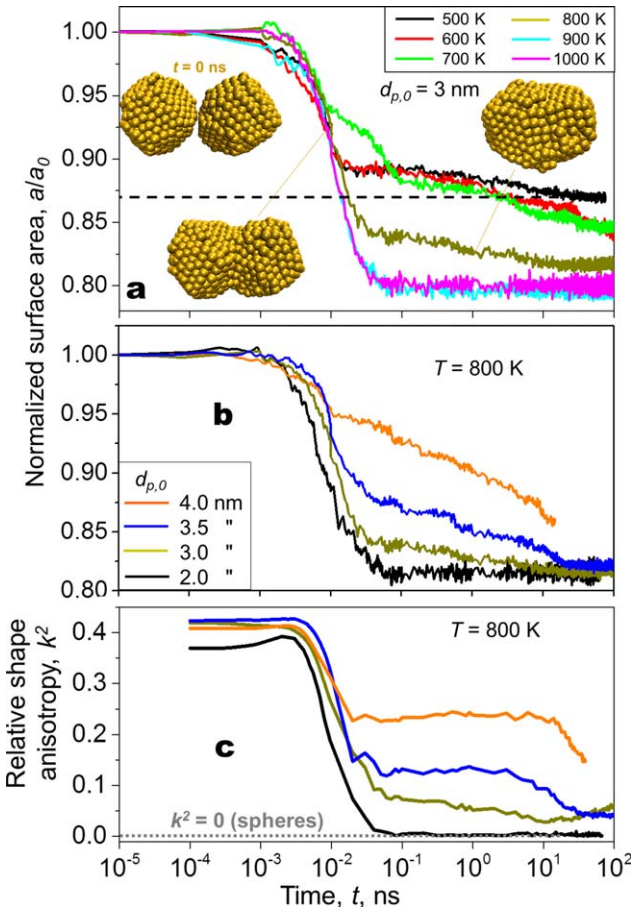

Figure 3. Evolution of normalized surface area of two Au nanoparticles undergoing sintering or coalescence

(a) at various temperatures and of initial $d_{p,0} = 3$ nm with their snapshots at $t = 0$, 0.01 and 1 ns for $T = 800$ K (insets) and (b) at various initial $d_{p,0}$ and $T = 800$ K. The broken line (Figure 3a) indicates the characteristic sintering time, τ_s, defined as the time needed for the excess surface area over that of an equivalent sphere to decrease by 67%. Increasing particle size or decreasing T lead to slower coalescence and decay of the normalized surface area. Figure 3c shows the evolution of the relative shape anisotropy, k^2, that nicely shows the levelling-off of the oval-shaped particles and the attainment of perfect spherical structures ($k^2 = 0$, dotted line) for $d_{p,0} = 2$ nm, at long t. [Color figure can be viewed in the online issue, which is available at wileyonlinelibrary.com.]

Figure 2 shows the melting temperature, T_m, of Au nanoparticles as function of their diameter for $d_{p,0} = 1.5$, 2, 3, 3.5, 4, 4.5, 5, 6, 7, 8, and 11 nm as obtained by the evolution of the Lindemann index (open circles) or potential energy per atom (filled circles). Both methods indicate that increasing particle size increases T_m which gradually approaches that of bulk Au, $T_{m,b} = 1337$ K (broken line). The T_m by the potential energy method is constantly lower than that obtained by the Lindemann index, consistent with Shibuta and Maruyama.[46] The results are in excellent agreement with theory (□: Lewis et al.[16]; ◇: Shim et al.[47]; Δ: Arcidiacono et al.[36];▽: Shibuta and Suzuki[48]) and experiments (Sambles[49]: dotted line; Buffat and Borel[50]: solid line). The bulk Au melting temperature is determined based on the abrupt change of the potential energy per atom and is close (within 4%) to the theoretical value of 1337 K (broken line).

Sintering rate of two gold nanoparticles

Figure 3a shows the evolution of the surface area, a, for two coalescing Au nanoparticles ($d_{p,0} = 3$ nm), normalized by their initial surface area, a_0, for $T = 500$–1000 K (solid lines) in the canonical (NVT) ensemble. Snapshots of the coalescing particles at $T = 800$ K are shown at $t = 0$, 0.01, and 1 ns (Figure 3a, insets). Initially ($t \approx 10^{-5}$–10^{-3} ns), the particles approach each other (adhesion) forming a neck of increasing size while the accessible surface area decreases ($t > 10^{-3}$ ns). The evolution of the normalized surface area follows the same trend for all T up to $t = 0.01$ ns and accelerates with increasing sintering temperature. Higher T results in faster sintering, consistent with the literature.[37] At sufficiently long times and high temperatures, particles attain a spherical-like shape and a/a_0 levels off to 0.79. Sintering takes place here in two stages: first, by particle adhesion and neck formation and growth where the cluster's free surface area decreases steeply and, second, by shape reformation where particle evolves from ellipsoidal to spherical-like indicated by slow surface area reduction. The trend of the surface evolution is similar to that of 2 nm-TiO_2 nanoparticles.[21] It should be noted that this sintering mechanism differs from the so-called attractive migration and coalescence where atom diffusion over the support facilitates neck formation and coarsening.[51] Here, sintering of free-standing nanoparticles in close proximity to each other (0.3 nm) was investigated as encountered in aerosol formation by coagulation and sintering of TiO_2[21] and Ag.[22]

Figure 3b shows the evolution of a/a_0 for starting particle diameters, $d_{p,0} = 2$ (black line), 3 (yellow line), 3.5 (blue line), and 4 nm (orange line) during sintering at $T = 800$ K. For $d_{p,0} = 2$ nm the surface area quickly ($t = 0.1$ ns) reaches a plateau due to rapid particle coalescence. Increasing particle size

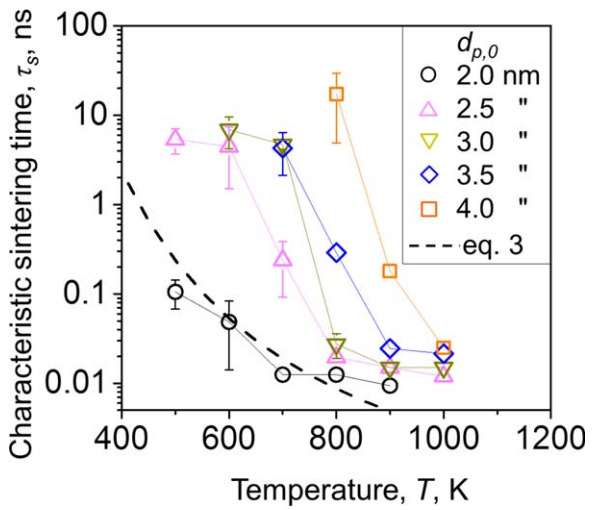

Figure 4. Characteristic sintering time, τ_s (open symbols) of two equally sized coalescing Au nanoparticles of initial, $d_{p,0}$, as a function of temperature.

The error bars show the minimum and maximum value of four simulations. Increasing temperature accelerates coalescence consistent with experiments.[37] The MD-obtained τ_s is in good agreement with the predictions of sintering by surface diffusion (broken line: Nichols and Mullins[40]; Nichols[54]; Lewis et al.[16]) for small particle sizes ($d_{p,0} = 2$ nm). [Color figure can be viewed in the online issue, which is available at wileyonlinelibrary.com.]

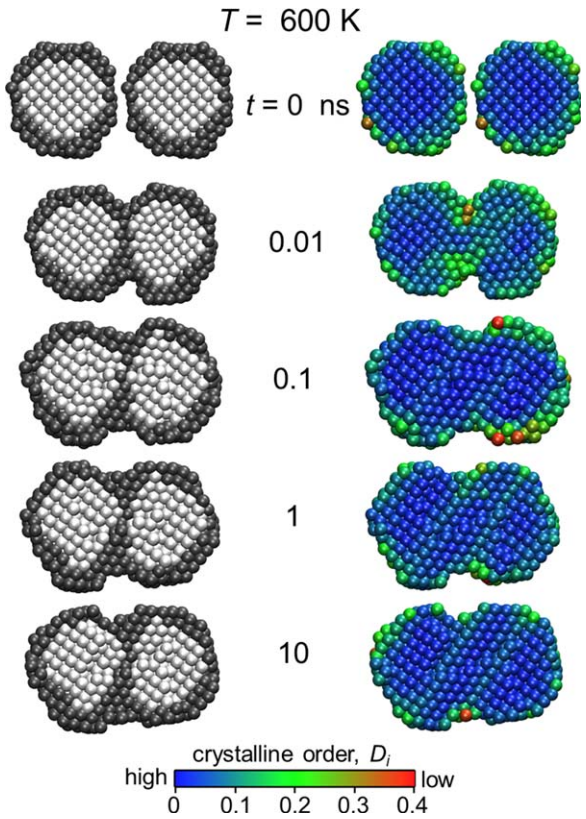

Figure 5. Snapshots of cross-sections of two Au nanoparticles with $d_{p,0} = 3$ nm at 600 K, at $t = 0$, 0.01, 0.1, 1, and 10 ns.

The atoms are colored based on their initial position (surface: gray, bulk: white) in the particle (left column) or based on their local disorder variable (blue to red atoms have increasing disorder variable; right column). Initially, particle adhesion takes place forming a neck ($t = 0.01$ ns), which continuously grows and finally disappears due to relocation of surface atoms ($t = 0.1 - 10$ ns). At the initial stages of sintering ($t = 0 - 0.1$ ns) the surface atoms have disordered structure while the bulk ones keep their fcc-like structure which finally dominates. [Color figure can be viewed in the online issue, which is available at wileyonlinelibrary.com.]

leads to slower reduction of the normalized surface area, consistent with experiments of Au particle evaporation.[52] For larger particles, adhesion takes longer than for smaller ones as bigger sinter necks are formed.

Figure 3c shows the evolution of the relative shape anisotropy, k^2, quantifying the sphericity of the particles of Figure 3b at $T = 800$ K. Large k^2 values correspond to linear-like structures (for perfect lines k^2 is 1) while for spheres $k^2 = 0$.[53] Initially, when particles have not formed yet a neck $k^2 \approx 0.4$, but during adhesion k^2 decreases abruptly similar to the evolution of the normalized surface area and levels off when particles attain an oval shape. For $d_{p,0} = 2$ nm (black line), the k^2 increases initially ($t \sim 0.001$ ns) corresponding to the early stages of particle adhesion where atoms on the adjacent particle surfaces are attracted to each other slightly elongating the particles. This is more dominant for the smallest particles as surface atoms dominate their behavior and slightly increase their anisotropy. On adhesion ($t = 0.005$ ns), such anisotropy reaches a maximum that decreases with the progression of coalescence and neck size growth as particle centers approach each other ($t = 0.01$ ns) (see also Supporting Information: Figure S1).

It takes a long time for such particles to become fully compact and even longer to become crystalline. Such time increases with increasing particle size and decreasing temperature. For example, particles with $d_{p,0} = 2$ nm (Figure 3c, black lines) have become spherical ($k^2 = 0$) already at 0.1 ns (but are amorphous) while larger ones are still elongated. It should be noted that formation of dumbbell-shaped particles appears to be the result of incomplete sintering that typically forms the so-called aggregates consisting of sinter-bonded primary particles that are quite attractive in catalysis, lightguide preforms, and nanoelectronics.[11]

Figure 4 shows the τ_s (open symbols) of coalescing Au nanoparticles with $d_{p,0} = 2$ (circles), 2.5 (triangles), 3 (inverse triangles), 3.5 (diamonds), and 4 nm (squares) as a function of the sintering temperature. The error bars show the minimum and maximum values of four simulations. For a given particle size, increasing T results in faster sintering, consistent with experiments[37] and, similarly, at a given T sintering takes longer with increasing particle size due to decreasing surface-to-volume ratio. The MD-obtained τ_s for $d_{p,0} = 2$ nm follows the evolution of sintering by surface diffusion (Eq. 3: broken line; Nichols and Mullins[40]; Nichols[54]; Lewis et al.[16]) indicating that particles aggregate by surface atom migration toward the neck region. At sufficiently high temperatures (above the melting point of each particle size), τ_s approaches an asymptotic

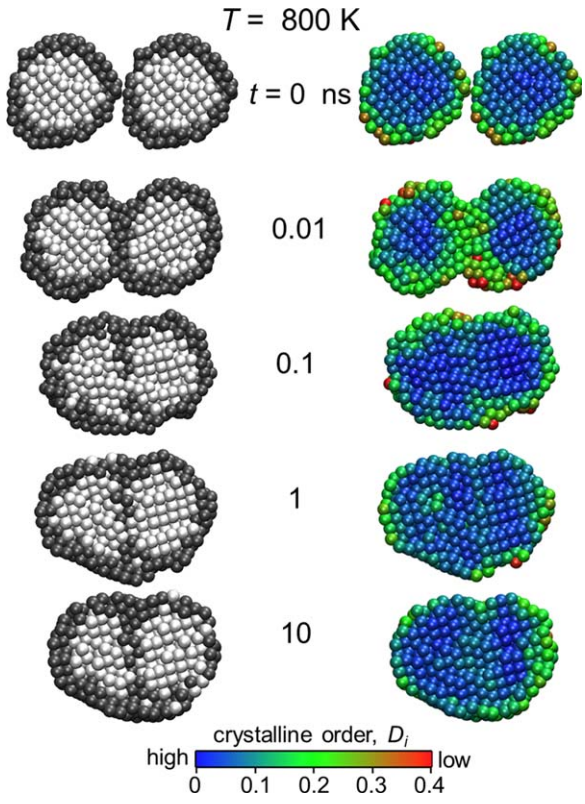

Figure 6. Snapshots of cross-sections of two Au nanoparticles with $d_{p,0} = 3$ nm at 800, K at $t = 0$, 0.01, 0.1, 1, and 10 ns, colored according to their initial position or their local disorder variable, as discussed in Figure 5.

Here, more atoms exhibit distorted crystal structure at all times compared with 600 K, while coalescence is completed already at the subnanosecond scale ($t = 0.1$ ns). [Color figure can be viewed in the online issue, which is available at wileyonlinelibrary.com.]

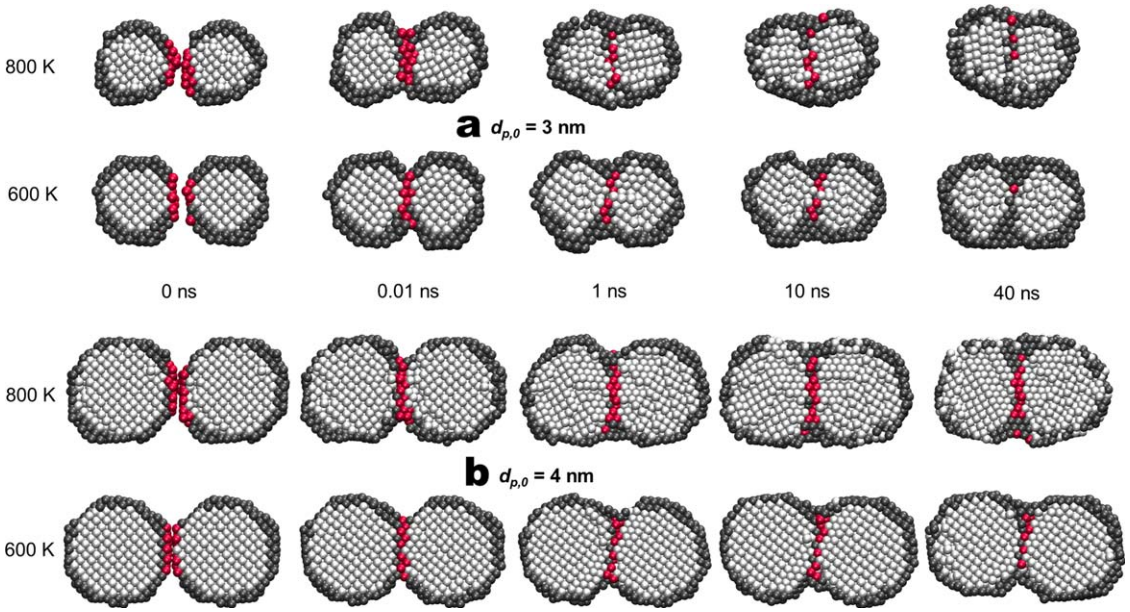

Figure 7. Snapshots of cross-sections of two coalescing Au nanoparticles with $d_{p,0}$ of

(a) 3 and (b) 4 nm for 800 (top) and 600 K (bottom) at $t = 0$, 0.01, 1, 10, and 40 ns. The atoms are colored based on their initial position in the particle as in Figure 5, and the atoms close to the neck region are colored in pink. Before particle adhesion ($t < 0.01$ ns) the atoms near the neck region are more mobile than both the bulk and surface atoms for $T = 600$ K, contrary to longer times that the neck atoms are "locked" inside the newly formed cluster (Figure 7a, bottom: $t \geq 10$ ns). At $T = 800$ K, the "neck atoms" initially remain in the bulk but as time elapses they diffuse towards the particle surface (top: $t \geq 10$ ns). This indicates further that at sufficiently low temperatures sintering takes place by surface diffusion, in the absence of grain boundary diffusion. [Color figure can be viewed in the online issue, which is available at wileyonlinelibrary.com.]

value where all shown particles ($d_{p,0} = 2$–4 nm) are amorphous and all atoms have similar mobility, consistent with simulations of coalescing Ag nanoparticles.[22] The above asymptotic τ_s is in agreement with MD simulations[55] of amorphous ($T = 1400$ K) Au nanoparticles with $d_{p,0} = 2.5$ and 3.5 nm giving τ_s of 0.03 and 0.04 ns, respectively.

Effect of temperature on atom mobility and crystallinity during sintering

MD simulations allow real-time analysis of dynamic properties that cannot be obtained easily by experiments, especially for small nanoparticles in the gas phase. Crystallinity dynamics considerably affect final product performance in a score of applications (e.g., sensors, catalysts, biomaterials, etc.) and are elucidated here for a range of particle sizes and sintering temperatures. Figure 5 shows snapshots of cross-sections of coalescing Au nanoparticles with $d_{p,0} = 3$ nm at 600 K, at $t = 0$, 0.01, 0.1, 1, and 10 ns. The particles are colored based on their initial ($t = 0$ ns) position (surface: gray, bulk: white) in the particle (left side) to trace their individual trajectories during sintering[21] or based on their local disorder variable, D_i (Eq. 6, right side), so that fcc-like structured atoms are blue (high crystalline order, $D_i \sim 0$) and disordered ones that deviate from the fcc structure are red (low crystalline order, $D_i \sim 0.4$).

Initially, particle adhesion takes place forming a neck ($t = 0.01$ ns) that continuously grows by migration of surface atoms towards the neck concave region (gray atoms fill up the area in between particles) that eventually disappears as an oval structure develops.[21] During the initial stages of sintering ($t = 0$–0.1 ns) the particle surface and neck region consist of disordered atoms of low crystallinity up to about 0.1 ns while the bulk atoms have fcc structure throughout the sintering process which finally dominates as the coalesced particle attains a more compact shape. For longer times ($t = 10$ ns), the initially bulk (white) atoms remain "trapped" surrounded by surface atoms as with TiO_2.[21] At $t = 1$ ns, twin boundaries are formed separating the cluster in three regions of different grain orientation (polycrystalline particle) which persists at $t = 10$ ns (see also Figure 8).

Figure 6 shows the Au nanoparticles of Figure 5 coalescing at $T = 800$ K. Here, particles have a thicker layer of disordered (amorphous) surface atoms than at lower T (e.g., 600 K), at all times. For example, at $t = 0.01$ ns, the neck region exhibits rather disordered (green to red: low crystalline order) structure which crystallizes as sintering proceeds ($t \geq 0.1$ ns), consistent with Liu et al.[38] The relocation rate of the surface atoms depends on sintering temperature (Eq. 3): at $T = 600$ K (Figure 5) coalescence is slow ($t = 0.1$–10 ns) while at $T = 800$ K (Figure 6) is completed already at the subnanosecond scale ($t = 0.1$ ns). However, at $t = 10$ ns, few of the bulk atoms have diffused toward the particle's surface at $T = 800$ K, in contrast to $T = 600$ K where bulk atoms have low mobility, as has been observed also for Ag.[22]

Figure 7 shows snapshots of cross-sections of two Au nanoparticles with $d_{p,0}$ of (a) 3 and (b) 4 nm undergoing sintering at 800 (top) and 600 K (bottom) at $t = 0$, 0.01, 1, 10, and 40 ns. The atoms are colored based on their initial position as in Figure 5 (left column), but the atoms close to the particle neck region are colored in pink. Thus, the trajectory of surface, neck, and bulk atoms is tracked providing insight to the detailed sintering mechanism and atom trajectories during sintering or coalescence. Neck and bulk atoms exhibit low mobility and oscillate around their initial position up to 1 ns while surface atoms are more mobile, consistent with calculations of their mean square displacement,[56] so they tend to occupy the space near the neck concave region, especially for $d_{p,0} = 3$ nm at both T. This indicates that sintering is initially dominated by surface diffusion,

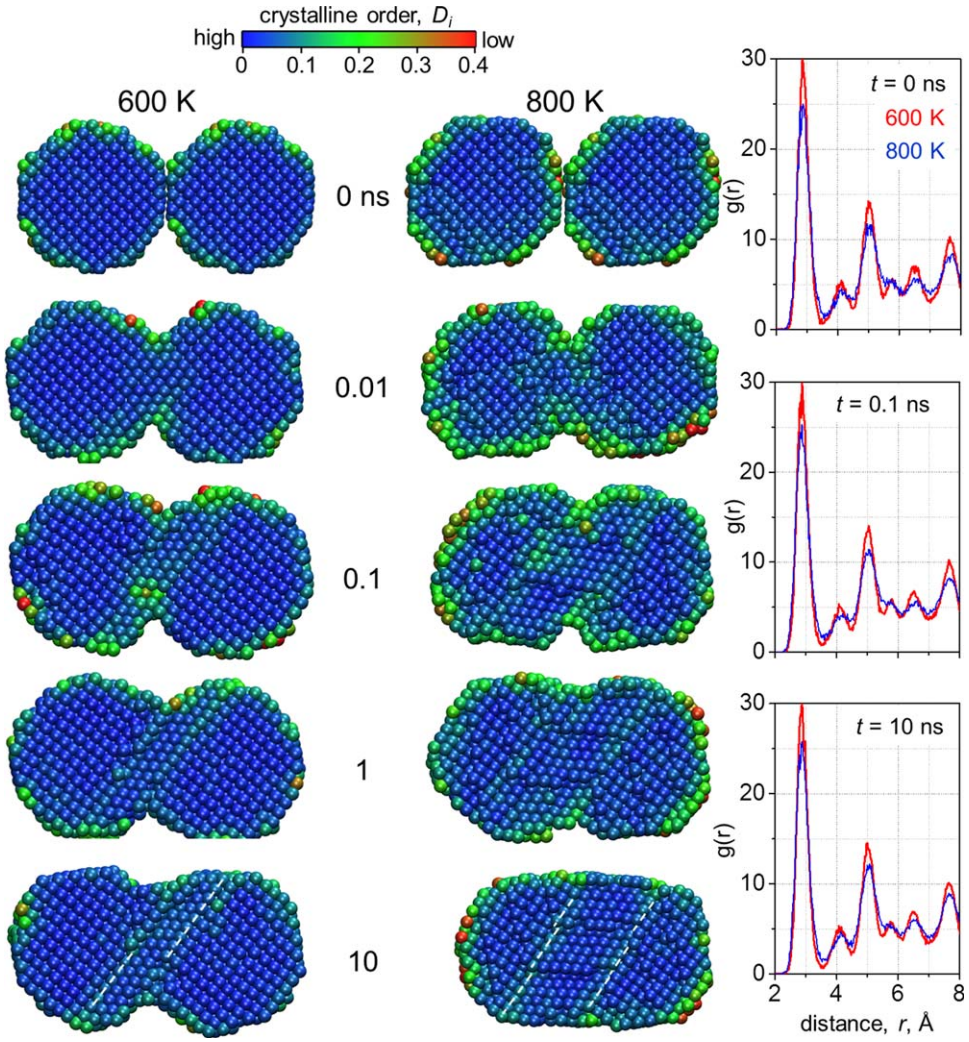

Figure 8. Snapshots of cross-sections colored according to the local disorder variable for two Au particles with $d_{p,0} = 4$ nm undergoing sintering at $T = 600$ (left column) and 800 K (right column) at $t = 0$, 0.01, 0.1, 1, and 10 ns.

The atoms of bigger particles (here 4 nm) exhibit fcc-like structure to a greater extent during adhesion compared with smaller ones (e.g., Figures 5 and 6) due to the reduced surface-to-volume ratio, resulting in lower values of the average disorder variable. The formation of grains with different orientation starts taking place for $t > 1$ ns. The radial distribution function, $g(r)$, is shown for 600 (red lines) and 800 K (blue lines) at $t = 0$, 0.1, and 10 ns. The peaks of $g(r)$ become slightly broader at $t = 0.1$ ns, providing a further indication of the reduced particle crystallinity at that time, consistent with Grammatikopoulos et al.[58] [Color figure can be viewed in the online issue, which is available at wileyonlinelibrary.com.]

consistent with sintering of TiO_2 nanoparticles.[21] Later on ($t > 1$ ns), however, neck (pink) atoms of the 3 nm particles at 800 K (Figure 7a: top) escape the core region and diffuse to the particle surface. At 600 K and same particle size though, sintering occurs solely by surface diffusion, as shown in Figure 7a (bottom) at $t = 40$ ns, where only surface atoms have occupied the neck region.

For larger (e.g., 4 nm) particles (Figure 7b), the sintering rate is slower (as shown in Figures 3 and 4) and the two particles are distinguishable up to 1 (800 K: top) or even 40 ns (600 K: bottom). At 800 K and 10 ns (Figure 7b), the surface atoms migrate toward the neck area while the initially bulk atoms diffuse to the particle shell. At even longer times ($t = 40$ ns), pink atoms are found to the particle surface, similar to $d_{p,0} = 3$ nm at 800 K (Figure 7a), revealing that surface diffusion prevails as a result of highly mobile surface atoms. So, the neck atoms are "locked" inside the newly formed cluster and diffuse away only at sufficiently long times and high temperatures similar to bulk atoms, a trend that is exacerbated with increasing particle diameter.[21]

The MD-obtained interatomic distances between surface–surface and bulk–bulk atoms differ up to 3.5% for $T = 600$ K. More specifically, surface atoms have smaller interatomic distance from the bulk ones due to lower coordination number. Variations in the interatomic distances have been observed also depending on the particle size (Zanchet et al.[57]; Supporting Information: Table S1).

Figure 8 shows snapshots of cross-sections of Au nanoparticles with $d_{p,0} = 4$ nm undergoing sintering at 600 (left column) and 800 K (right column) at $t = 0$, 0.01, 0.1, 1, and 10 ns, as well as their corresponding radial distribution function, $g(r)$. Similar to Figures 5 and 6, surface atoms are more mobile (or liquid-like) than bulk ones and, thus, they exhibit higher degree of disorder (color coding same as in Figure 5), especially at 800 K. However, a bigger fraction of atoms attains the fcc-like structure compared with $d_{p,0} = 3$ nm

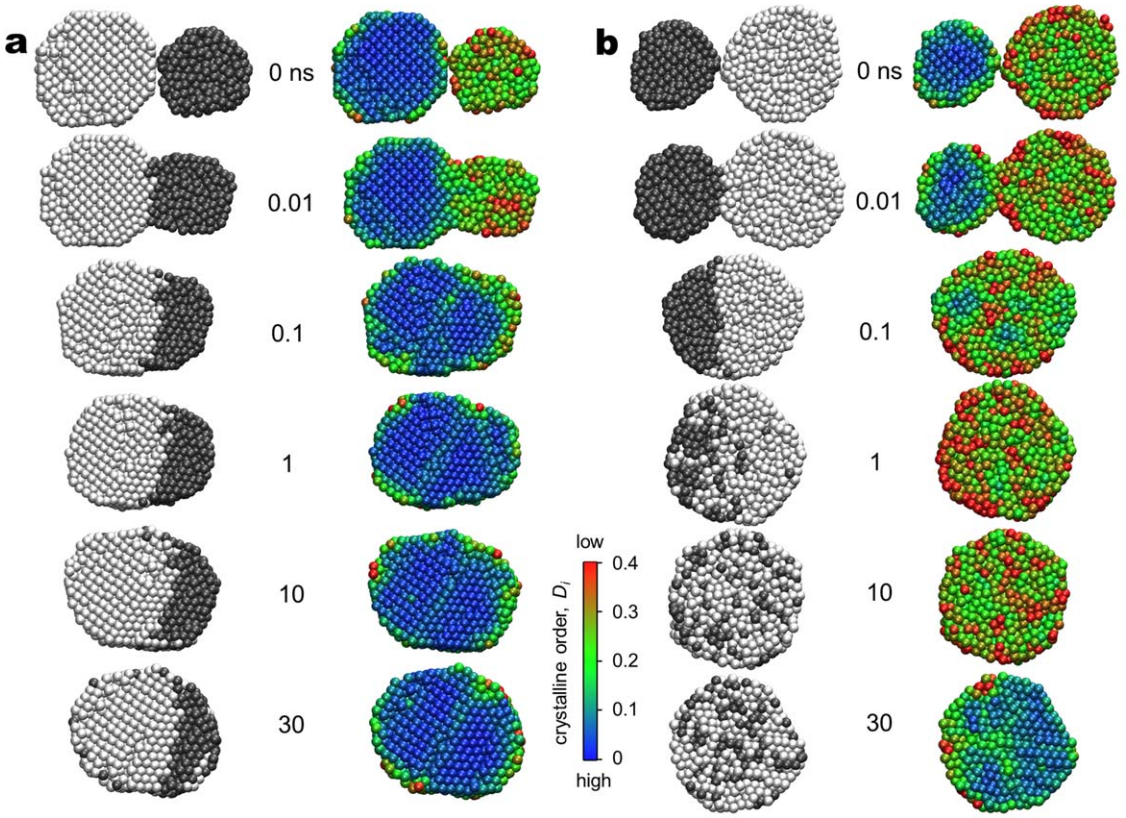

Figure 9. Snapshots of cross-sections of two Au nanoparticles with $d_{p,0} = 3$ (gray) and 4 nm (white) undergoing sintering at $T = 800$ K at $t = 0$, 0.01, 0.1, 1, 10, and 30 ns.

Even though the smaller particle is initially amorphous (Figure 9a) when sintering starts taking place, it attains the crystal structure and grain orientation of the bigger particle. However, when the bigger particle is initially amorphous (Figure 9b) the resulting cluster also has low crystalline order ($t \leq 10$ ns), but at sufficiently long times ($t = 30$ ns) recrystallization occurs and multiple grains are formed that grow with time. [Color figure can be viewed in the online issue, which is available at wileyonlinelibrary.com.]

(Figures 5 and 6) due to the smaller surface-to-volume ratio resulting in a reduction in the average disorder variable (as shown for $d_{p,0} = 3$ and 3.5 nm, Supporting Information: Figure S2). The formation of grains with different orientation starts taking place at $t = 1$ ns while later on ($t = 10$ ns) twin boundaries are formed indicated here by the white broken lines. Such twin boundary formation has been observed by *in situ* TEM of coalescing Au nanoparticles ($d_{p,0} = 3$–7 nm) by electron beam irradiation, as a result of particle rotation to achieve alignment of their crystallographic orientations (Yuk et al.[23]: Figure 1). Here, however, grain boundary diffusion does not take place as the grain boundaries do not propagate. The $g(r)$ is shown at 600 K (red lines) and 800 K (blue lines) at $t = 0$, 0.1, and 10 ns. The first peak of the $g(r)$ function (peak of the nearest neighbor atoms) is broader for 800 K, revealing the decreased crystallinity order at that T. This peak becomes slightly broader even at the same T, when particle adhesion and neck growth take place ($t = 0.1$ ns), indicating further the enhanced degree of disorder at that stage, consistent with MD simulations of Pd nanoparticles (Grammatikopoulos et al.[58]: Figure 9).

Effect of initial crystal structure on crystallinity dynamics during sintering

Figure 9 shows snapshots of cross-sections of two unequally sized coalescing Au nanoparticles with $d_{p,0} = 3$ (gray) and 4 nm (white) at $t = 0$, 0.01, 0.1, 1, and 10 ns. The atoms are colored based on the particle they initially belong to (left columns) or based on the value of their disorder variable (right columns). To eliminate the effect of initial crystal structure on the orientation of the formed grain, the smaller particle has amorphous structure (no "blue" atoms exist at this temperature) while the bigger one is crystalline (Figure 9a). The two particles undergo sintering at $T = 800$ K. After adhesion, the atoms of the small, liquid-like particle align with those of the bigger particle and form a new grain of similar orientation with the starting particle ($t > 0.1$ ns). This eventual propagation of the crystalline structure (big particle) toward largely disordered domains (small particle) results in structures similar to those formed by grain boundary migration (Yuk et al.[23]: Figure 2). It should be noted that our simulations with unsupported Au nanoparticles are in qualitative agreement with the data of Yuk et al.[23] of supported Au nanoparticles despite the difference in temperature and time scale as electron beam irradiation may heat the particles to high enough temperature to induce their sintering.

In Figure 9b, the initial fraction of crystalline particles is decreased by starting with a small, crystalline particle ($d_{p,0} = 3$ nm) and a big, amorphous one. The nanoparticles sinter at constant $T = 800$ K and rapidly ($t = 0.1$ ns) form a spherical amorphous particle. This liquid-like phase persists ($t = 10$ ns) until recrystallization takes place ($t = 30$ ns) and multiple twins are formed (polycrystalline particle). Furthermore, sintering is faster here (Figure 9b) as full coalescence is completed at $t = 0.1$ ns, contrary to the initial configuration of high crystalline order (Figure 9a) that particle rounding takes longer.

Figure 10 shows the evolution of normalized surface area of two Au nanoparticles of equal (3–3 or 4–4 nm) and different

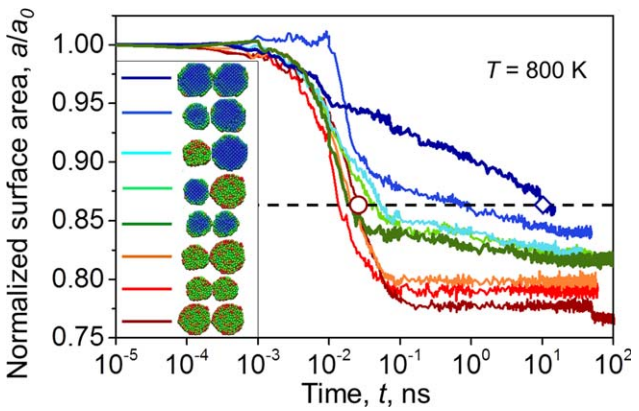

Figure 10. Evolution of normalized surface area of two Au nanoparticles of equal (3–3 or 4–4 nm) and different diameters (3–4 nm) undergoing sintering or coalescence at $T = 800$ K.

Initially ($t = 0$ ns), the particles have different crystalline structure which affects the evolution of surface area reduction and therefore the sintering rate. For example, the 4–4 nm crystalline nanoparticles (dark blue line) coalesce much more slowly than amorphous ones of the same size (brown line) and the corresponding τ_s differ more than two orders of magnitude (open symbols). [Color figure can be viewed in the online issue, which is available at wileyonlinelibrary.com.]

diameters (3–4 nm) undergoing sintering or coalescence at $T = 800$ K. Initially ($t = 0$ ns), the particles have different crystallinity state (amorphous or relatively high crystalline order) that affects the evolution of surface area reduction and, therefore, the sintering rate, especially for large particle sizes. For example, the 4–4 nm crystalline nanoparticles (dark blue line) coalesce much more slowly ($\tau_s \approx 10$ ns, diamond) than amorphous ones of the same size (brown line) that the corresponding τ_s is more than two orders of magnitude smaller ($\tau_s \approx 0.025$ ns, circle). So, amorphous nanoparticles sinter much faster than crystalline ones for given particle size and temperature. Thus, the crystal structure of Au coalescing nanoparticles not only affects the sintering mechanism[23] but also the rate of sintering or coalescence.

Conclusions

The sintering rate and crystallinity dynamics of coalescing Au nanoparticles are investigated by MD at isothermal conditions for various particle sizes. The trajectories of the neck, surface, and bulk atoms reveal that early sintering primarily takes place by surface diffusion due to the increased mobility of surface atoms, in the absence of grain boundary diffusion.

The crystallinity dynamics are elucidated during sintering of different Au particle sizes and initial crystalline configurations, using a disorder variable that quantifies the local crystal structure. Surface atoms are highly distorted (amorphous), especially for small particles and high temperatures, while bulk atoms generally retain their fcc structure throughout the process. During particle adhesion, the atoms close to the neck region exhibit low crystalline order but recrystallize as sintering proceeds, consistent with literature. At early stages of sintering, grains of different orientation are formed. Coalescing particles of diverse initial crystallinity result in polycrystalline materials (multiple twin boundaries) that form by different sintering rates, even though formation of completely amorphous particles is observed before recrystallization takes place.

Acknowledgments

The research leading to these results has received funding from the Swiss National Science Foundation (grant no. 200021_149144) and the European Research Council under the European Union's Seventh Framework Programme (FP7/2007-2013, ERC grant agreement no. 247283). For this research, E. Goudeli received a best poster award from the Particle Technology Forum at the 2015 AIChE Annual Meeting in Salt Lake City, UT, Nov. 8–13.

Literature Cited

1. Haruta M, Yamada N, Kobayashi T, Iijima S. Gold catalysts prepared by coprecipitation for low-temperature oxidation of hydrogen and of carbon monoxide. *J Catal*. 1989;115:301–309.
2. Liedberg B, Nylander C, Lundstrom I. Surface plasmon resonance for gas detection and biosensing. *Sensor Actuat*. 1983;4:299–304.
3. Hirsch LR, Stafford RJ, Bankson JA, Sershen SR, Rivera B, Price RE, Hazle JD, Halas NJ, West JL. Nanoshell-mediated near-infrared thermal therapy of tumors under magnetic resonance guidance. *PNAS*. 2003;100:13549–13554.
4. Zheng J, Chen Z, Liu Z. Atomic force microscopy-based nanolithography on silicon using colloidal Au nanoparticles as a nanooxidation mask. *Langmuir*. 2000;16:9673–9676.
5. Ye BC, Yin BC. Highly sensitive detection of Mercury(II) Ions by fluorescence polarization enhanced by gold nanoparticles. *Angew Chem Int Ed*. 2008;47:8386–8389.
6. Brust M, Kiely CJ. Some recent advances in nanostructure preparation from gold and silver particles: a short topical review. *Colloid Surface A*. 2002;202:175–186.
7. Fujita T, Guan P, McKenna K, Lang X, Hirata A, Zhang L, Tokunaga T, Arai S, Yamamoto Y, Tanaka N, Ishikawa Y, Asao N, Yamamoto Y, Erlebacher J, Chen M. Atomic origins of the high catalytic activity of nanoporous gold. *Nature Mater*. 2012;11:775–780.
8. Cushing BL, Kolesnichenko VL, O'Connor CJ. Recent advances in in the liquid-phase syntheses of inorganic nanoparticles. *Chem Rev*. 2004;104:3893–3946.
9. Kruis EF, Fissan H, Peled A. Synthesis of nanoparticles in the gas phase for electronic, optical and magnetic applications—A review. *J Aerosol Sci*. 1998;29:511–535.
10. Turkevich J, Stevenson PC, Hillier J. A study of the nucleation and growth processes in the synthesis of colloidal gold. *Discuss Faraday Soc*. 1951;11:55–75.
11. Pratsinis SE. Aerosol-based technologies in nanoscale manufacturing: from functional materials to devices through core chemical engineering. *AIChE J*. 2010;56:3028–3035.
12. Buesser B, Pratsinis SE. Design of nanomaterial synthesis by aerosol processes. *Ann Rev Chem Biomol Eng*. 2012;3:103–127.
13. Tang Y, Ouyang M. Tailoring properties and functionalities of metal nanoparticles through crystallinity engineering. *Nature Mater*. 2007;6:754–759.
14. Yip S. Nanocrystals: the strongest size. *Nature*. 1998;391:532–533.
15. Zhu H, Averback RS. Sintering process of two nanoparticles: a study by molecular dynamics simulations. *Phil Mag Lett*. 1996;73:27–33.
16. Lewis LJ, Jensen P, Barrat J-L. Melting, freezing, and coalescence of gold nanoparticles. *Phys Rev B*. 1997;56:2248–2257.
17. Raut JS, Bhagat RB, Fichthorn KA. Sintering of aluminum nanoparticles: a molecular dynamics study. *Nanostruct Mater*. 1998;10:837–851.
18. Zachariah MR, Carrier MJ. Molecular Dynamics computation of gas-phase nanoparticle sintering: a comparison with phenomenological models. *J Aerosol Sci*. 1999;30:1139–1151.
19. Zhao SJ, Wang SQ, Yang ZQ, Ye HQ. Coalescence of three silver nanoclusters: a molecular dynamics study. *J Phys Condens Mat*. 2001;13:8061–8069.
20. Koparde VN, Cummings PT. Molecular dynamics simulation of titanium dioxide nanoparticle sintering. *J Phys Chem B*. 2005;109:24280–24287.
21. Buesser B, Gröhn AJ, Pratsinis SE. Sintering rate and mechanism of TiO_2 nanoparticles by molecular dynamics. *J Phys Chem C*. 2011;115:11030–11035.
22. Buesser B, Pratsinis SE. Morphology and crystallinity of coalescing nanosilver by molecular dynamics. *J Phys Chem C*. 2015;119:10116–10122.
23. Yuk JM, Jeong M, Kim SY, Seo HK, Kim J, Lee JY. *In situ* atomic imaging of coalescence of Au nanoparticles on graphene: rotation and grain boundary migration. *Chem Commun*. 2013;49:11479–11481.

24. Valden M, Lai X, Doodman DW. Onset of catalytic activity of gold clusters on titania with the appearance of nanometallic properties. *Science*. 1998;281:1647–1650.
25. Fujiwara K, Deligiannakis Y, Skoutelis CG, Pratsinis SE. Visible-light active black TiO_2-Ag/TiO_x particles. *Appl Catal B*. 2014;154:9–15.26.
26. Swope WC, Anderson HC, Berens PH, Wilson KR. A computer simulation method for the calculation of equilibrium constants for the formation of physical clusters of molecules: Application to small water clusters. *J Chem Phys*. 1982;76:637–649.
27. Daw M, Baskes M. Semiempirical, quantum-mechanical calculation of hydrogen embrittlement in metals. *Phys Rev Lett*. 1983;50:1285–1288.
28. Daw M, Baskes M. Embedded-atom-method—derivation and application to impurities, surfaces and other defects in metals. *Phys Rev B*. 1984;29:6443–6453.
29. Foiles S, Baskes M, Daw M. Embedded-Atom-Method functions for the fcc metals Cu, Ag, Au, Ni, Pd, Pt, and their alloys. *Phys Rev B*. 1986;33:7983–7991.
30. Plimpton S. Fast parallel algorithms for short-range molecular dynamics. *J Comput Phys*. 1995;117:1–19.
31. Sanner MF, Olson AJ, Spehner JC. Reduced surface: an efficient way to compute molecular surfaces. *Biopolymers*. 1995;38:305–320.
32. Bondi A. van der Waals Volumes and Radii. *J Phys Chem*. 1964;68:441–451.
33. Brunauer S, Emmett PH, Teller E. Adsorption of gases in multimolecular layers. *J Am Chem Soc*. 1938;60:309–319.
34. Kobata A, Kusakabe K, Morooka S. Growth and transformation of TiO_2 crystallites in aerosol reactor. *AIChE J*. 1991;37:347–359.
35. Koch W, Friedlander SK. The effect of particle coalescence on the surface area of a coagulating aerosol. *J Colloid Interface Sci*. 1990;140:419–427.
36. Arcidiacono S, Bieri NR, Poulikakos D, Grigoropoulos CP. On the coalescence of gold nanoparticles. *Int J Multiphas Flow*. 2004;30:979–994.
37. Nakaso K, Shimada M, Okuyama K, Deppert K. Evaluation of the change in morphology of gold nanoparticles during sintering. *J Aerosol Sci*. 2002;33:1061–1074.
38. Liu HB, José-Yacaman M, Perez R, Ascencio JA. Studies of nanocluster coalescence at high temperature. *Appl Phys A*. 2003;77:63–67.
39. Coblenz WS, Dynys JM, Canon RM, Colde RL. *Initial stage solid state sintering models. A critical analysis and assessment. Sintering Processes, Material Science Research*. New York: Plenum, 1980:141–157.
40. Nichols FA, Mullins WW. Morphological changes of a surface of revolution due to capillarity induced surface diffusion. *J Appl Phys*. 1965;36:1826–1835.
41. Steinhardt PJ, Nelson DR, Ronchetti M. Bond-orientational order in liquid and glasses. *Phys Rev B*. 1983;28:784–805.
42. Kawasaki T, Onuki A. Construction of a disorder variable from Steinhardt order parameters in binary mixtures at high densities in three dimensions. *J Chem Phys*. 2011:135:174109-1–174109–8.
43. Lechner W, Dellago C. Accurate determination of crystal structures based in average local bond order parameters. *J Chem Phys*. 2008;129:114707-1–114707–5.
44. Zhou Y, Karplus M, Ball KD, Berry RS. The distance fluctuation criterion for melting: comparison of square-well and morse potential models for clusters and homopolymers. *J Chem Phys*. 2002;116:2323–2329.
45. Alavi S, Thomson DL. Molecular dynamics of the melting of aluminum nanoparticles. *Science*. 1998;281:1647–1650.
46. Shibuta Y, Maruyama S. A molecular dynamics study of the effect of a substrate on catalytic metal clusters in nucleation process of single-walled carbon nanotubes. *Chem Phys Lett*. 2010;498:323–327.
47. Shim J-H, Lee B-L, Cho YW. Thermal stability of unsupported gold nanoparticle: a molecular dynamics study. *Surf Sci*. 2002;512:262–268.
48. Shibuta Y, Suzuki T. Melting and solidification point of fcc-metal nanoparticles with respect to particle size: A molecular dynamics study. *Chem Phys Lett*. 2010;498:323–327.
49. Sambles JR. An electron microscope study of evaporating gold particles: the Kelvin equation for liquid gold and the lowering of the melting point of solid gold particles. *Proc R Soc Lond A*. 1971;324:339–351.
50. Buffat P, Borel J-P. Size effect on the melting temperature of gold particles. *Phys Rev A*. 1976;13:2287–2298.
51. Yang WC, Zeman M, Ade H, Nemanich RJ. Attractive migration and coalescence: a significant process in the coarsening of TiSi2 islands on the Si(111) surface. *Phys Rev Lett*. 2003;90:136102-1–136102–4.
52. Nanda KK, Maisels A, Kruis FE. Surface tension and sintering of free gold nanoparticles. *J Phys Chem*. 2008;112:13488–13491.
53. Theodorou DN, Suter UW. Shape of unperturbed linear polymers: polypropylene. *Macromolecules*. 1985;18:1206–1214.
54. Nichols FA. Coalescence of two spheres by surface diffusion. *J Appl Phys*. 1966;37:2805–2808.
55. Pan H, Ko SH, Grigoropoulos CP. The coalescence of supported gold nanoparticles induced by nanosecond laser irradiation. *Appl Phys*. 2008;90:247–253.
56. Song P, Wen D. Molecular dynamics simulation of the sintering of metallic nanoparticles. *J Nanopart Res*. 2010;12:823–829.
57. Zanchet D, Tolentino H, Martins Alves MC, Alves OL, Ugarte D. Inter-atomic distance contraction in thiol-passivated gold nanoparticles. *Chem Phys Lett*. 2000;323:167–172.
58. Grammatikopoulos P, Cassidy C, Singh V, Sowwan M. Coalescence-induced crystallisation wave in Pd nanoparticles. *Sci Rep*. 2014;4:1–9.

Manuscript received Sep. 18, 2015, and revision received Nov. 29, 2015.